Enhanced cracking resistance and deposition of alloy 36 via accelerated cooling and TiC addition during wire arc additive manufacturing

Sood, Arjun; Bosman, Marko; Huizenga, Richard; Goulas, Constantinos; Popovich, Vera; Hermans, Marcel J.M.

Important note
To cite this publication, please use the final published version (if applicable).
Please check the document version above.

Enhanced cracking resistance and deposition of alloy 36 via accelerated cooling and TiC addition during wire arc additive manufacturing

Arjun Sood, Marko Bosman, Richard Huizenga, Constantinos Goulas, Vera Popovich & Marcel J. M. Hermans

Published online: 16 Apr 2025.

Submit your article to this journal ↗

View related articles ↗

View Crossmark data ↗

Taylor & Francis
Taylor & Francis Group

Enhanced cracking resistance and deposition of alloy 36 via accelerated cooling and TiC addition during wire arc additive manufacturing

Arjun Sood [a], Marko Bosman[b], Richard Huizenga[a], Constantinos Goulas [c], Vera Popovich [a] and Marcel J. M. Hermans [a]

aDepartment of Mechanical Engineering, Delft University of Technology, The Netherlands; bGKN Aerospace, Fokker Aerostructures B.V., The Netherlands; cFaculty of Engineering Technology, University of Twente, The Netherlands

ABSTRACT

The sensitivity of the single-phase, low thermal expansion (LTE) alloy 36 (Fe-36Ni) to intergranular cracking hinders its processability during additive manufacturing. This study investigates the effect of accelerated cooling via a CO_2 jet and the addition of TiC particles on the cracking susceptibility of the LTE36 alloy during wire-arc additive manufacturing (WAAM). Results show that accelerated cooling reduces inter-pass deposition times and the susceptibility to cracking due to increased heat dissipation. A crack-free microstructure was achieved only with the addition of TiC particles, which pinned the high-angle grain boundaries and induced tortuosity, thereby limiting grain growth and mitigating intergranular cracking. Mechanical performance was restored compared to the cracked condition, and the critical LTE property of the as-deposited LTE36 alloy was improved due to the enhanced ferromagnetic character of the alloy. Therefore, the combined approach effectively mitigated intergranular cracking while retaining the LTE behaviour during WAAM of the LTE36 alloy.

Introduction

The industrial demand for materials that maintain exceptional dimensional stability under varying thermal conditions is ever-increasing [1]. Specifically, the low thermal expansion 36 (LTE36, alloy 36 or Invar 36) alloy renowned for its remarkably low linear coefficient of thermal expansion (CTE), has found diverse applications across industries demanding high dimensional stability, such as aerospace, precision instruments, and cryogenic engineering [2,3]. The alloy's unique ability to maintain its dimensions over a wide range of temperatures makes it indispensable in environments where precision and reliability are paramount [4]. In particular, the aerospace industry relies on LTE36 alloy moulding tools during the curing process of composite material based aerospace structures. The minimal mismatch between the CTE of LTE36 alloy and composite materials ensures precise dimensional control of the composite structures during the curing process. For instance, the spring-back distortion of a 0.24 m carbon fibre composite aerospace antenna was shown to be approximately 20% lower when manufactured using a moulding tool made of

Invar 36, compared to a stainless steel AISI 430 tool [5]. Therefore, LTE36 alloy moulding tools enable the production of high-quality aerospace structures that retain their intended dimensionality after undergoing a curing cycle. However, the traditional part production of LTE36 alloy through the subtractive manufacturing route has faced challenges related to cost, material waste, and ability to create complex geometries [6,7].

Advancements in metal additive manufacturing (AM) have opened new avenues for fabricating the critical LTE36 alloy. In particular, wire arc additive manufacturing (WAAM) stands-out among metal AM processes for its ability to produce medium to large scale parts while maximising the deposition rates [8]. It relies on the use of an electric arc to melt wire-based feedstock materials, and offers significant advantages, including reduced feedstock material waste, shorter lead times and the ability to create complex shapes compared to traditional manufacturing methods [9–12]. Substantial research has been conducted in recent years to expand the potential of AM techniques in processing the LTE36 alloy [13–23]. Despite the successes of fabricating LTE36 alloy through

the AM route, multiple studies report the persistence of intergranular cracking in the deposited microstructures. Qiu et al. [24], observed the presence of cracks in as-printed and post-treated microstructures of LTE36 alloy deposited via selective laser melting. Tan et al. [25], employed laser metal deposition to fabricate LTE36 alloy specimens and reported the dependence of intergranular cracking on the laser scanning speed, given a constant laser power and spot diameter. Additionally, our previous work described the deposition of LTE36 alloy using WAAM at heat inputs (HI) ranging from 200 to 550 J mm^{-1} [26]. Except for the alloy deposited at the lowest HI setting, intergranular cracking was encountered at other HIs. In general, lowering the HI during WAAM reduces the susceptibility of intergranular crack-sensitive alloys to cracking. However, this approach compromises a crucial advantage of WAAM over other metal AM methods. The reduction in HI inherently decreases the deposition rate, thus undermining WAAM's ability to achieve high deposition rates. Therefore, it is essential to explore alternative strategies that mitigate cracking in LTE36 alloy during WAAM without relying on HI reduction.

The present study builds on our earlier work and aims to mitigate intergranular cracking during WAAM of LTE36 alloy at the higher extreme of HI, i.e. 550 J mm^{-1}. This is particularly relevant from a production perspective, as a higher HI translates to increased deposition rates. Moreover, it is also crucial from the standpoint of enhancing the mechanical properties, given that the presence of intergranular cracks has a deleterious impact on the tensile properties of LTE36 alloy. This work utilises gas tungsten arc welding (GTAW) in the pulsed current mode with front wire feeding for depositing the LTE36 alloy. To mitigate intergranular cracking from LTE36 alloy, our deposition approach comprises of supplying a solid CO_2 cooling jet through the substrate and applying a paste containing TiC particles between the deposited layers. The CO_2 jet was utilised to accelerate the dissipation of heat during WAAM, and the TiC particles were selected due to their high-temperature stability and fcc crystal (like LTE36 alloy) symmetry. Additionally, existing studies that have modified austenitic stainless steels by adding TiC during AM have consistently reported improved microstructural and functional performance of the alloy [27–29]. The effect of the cooling jet on the deposits was characterised by melt pool observations and measurements of the time-temperature curves. The microstructural response of the LTE36 alloy to the TiC particle addition was established through X-ray fluorescence (XRF), X-ray diffraction (XRD) and electron backscatter diffraction (EBSD) techniques. Lastly, mechanical and

dilatometric analysis were performed to quantify the functional performance of the as-deposited alloy. The results of this study demonstrate geometrically stable deposition of thick-wall LTE36 alloy structures at an increased HI, facilitated by the incorporation of a cooling jet during WAAM. When combined with TiC particle addition, this approach enables the defect-free fabrication of LTE36 alloy with improved functional performance compared to its conventional counterpart. Consequently, the present work enhances the utility of WAAM to deposit defect-free and functional LTE36 alloy with reasonable inter-pass times, which is particularly suited for fabricating moulding tools in the aerospace industry.

Research methodology

Alloy 36 deposition

The experiments were performed using a Migatronic TIG COMMANDER AC/DC 400 power source in the pulsed current mode. An independent wire feeding system supplied by Migatronic was used to deposit the LTE36 alloy wire. The wire is manufactured by voestalpine Böhler Welding and commercially known as 3Dprint AM Mold 36. The wire feeding system was attached to the electric arc torch, which was manipulated using a servo motor-controlled motion system. An inert shielding environment for the arc and the melt pool during the experiments was achieved using argon gas at a flow rate of 10 L min^{-1}. A non-consumable tungsten alloy electrode was used for generating an electric arc at a tip angle of 40° in negative polarity. The deposition process is schematically shown in Figure 1(a). The experiments comprised depositing five blocks of $80 \times 15 \times 15$ mm^3: a reference block without the use of the CO_2 jet and TiC powder particles, a block with accelerated CO_2 jet cooling, and three blocks with accelerated cooling and varying amounts of TiC particles. These blocks are summarised according to their deposition conditions in Table 1. The reference block and the blocks with TiC particles will be referred to as SR and SA to SC, respectively, while the block deposited with just accelerated cooling is referred to as SCL. The TiC powder particles were supplied by Sigma Aldrich and were of 99.9% purity with a size limitation of 325 mesh. The morphology of the TiC powder particles is shown in Figure 1(b). The powder was applied as a paste between successive passes (Figure 1(a)), the application method was adapted from other studies [30,31]. All the blocks were deposited on similar sized substrates of low carbon steel, 25 mm in thickness. A through hole of 8 mm diameter was drilled in the substrates used for blocks SA to SC to supply the
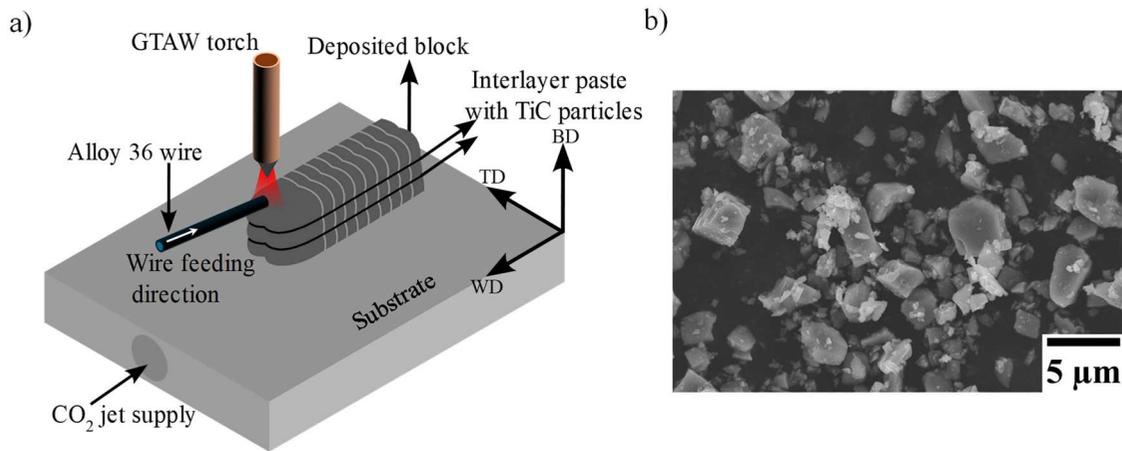
Figure 1. schematic diagram of the WAAM process employed in this study incorporating a CO_2 jet and interlayer paste with TiC particles in (a), where BD, TD, and WD are the building, transverse, and welding/travel directions, respectively. Morphology of the TiC particles used in the present work shown in (b).

Table 1. Overview of the deposition conditions for the blocks deposited in this study.

Blocks	Condition
Block SR	Reference
Block SCL	CO_2 cooling
Blocks SA to SC	Cooling and TiC

CO_2 jet during deposition. The thermal history during the deposition was recorded using K-type thermocouples connected to a YOKOGAWA DL 750 ScopeCorder data logger at a sampling rate of 1 kHz. The thermocouples were encased in ceramic holders to shield them from the electric arc and spot welded to the edge of the blocks at a height of 10 mm from the substrate. An inter-pass temperature of 70 ± 5 °C was maintained during the deposition.

Microstructure observation and analysis

Samples were extracted and prepared for microstructure observation from the deposited blocks using standard mechanical grinding (P180 to P4000 abrasive papers) and polishing (3 μm and 1 μm suspensions) procedures. Chemical etching was performed using Kalling's No. 2 reagent to reveal the grain structure. A Keyence VHX-5000 digital microscope was used for this purpose. A ThermoScientific™ Helios™ G4 Plasma FIB UXe (Helios) scanning electron microscope (SEM) was used to examine the microstructure of the samples in the polished condition. X-ray diffraction (XRD) was utilised for the purpose of phase identification and evaluation of the lattice parameters. A Bruker D8 Advance diffractometer was used to obtain the diffraction patterns followed by data

evaluation with DiffracSuite. EVA version 7.2 software. The instrument used Co K_α radiation with a step size of 0.035° 2θ and a counting time of 5 s per step during the scans. The additions of Ti and C were quantified through X-ray fluorescence (XRF) and LECO elemental analyser, respectively. A Panalytical Axios^{mAX} WD-XRF spectrometer was used to obtain the XRF spectra followed by data evaluation with SuperQ 5 software. Additionally, electron backscatter diffraction (EBSD) was performed for detailed analysis of the microstructure using the Helios SEM. This instrument is equipped with EDAX EBSD and energy dispersive spectroscopy (EDS) detectors and can be used for coupled microstructure-chemical composition analysis. Samples for EBSD were polished with a colloidal silica (OP-S) suspension for 25 minutes in addition to the earlier stated procedure. The samples were tilted to 60°, and a step size of 0.05 μm was used during the scans. The beam current and acceleration voltage during EBSD with simultaneous EDS measurements were 6.4 nA and 10 kV, respectively. Lastly, large-area EBSD scans were performed by utlising a JEOL 7200F field emission SEM equipped with an Oxford Instruments EBSD detector. The beam current and acceleration voltage during these scans were 3.2 nA and 15 kV, respectively, with a step size of 5 μm.

Mechanical testing

A larger block, referred to as block SDM, of $130 \times 15 \times 60$ mm^3 corresponding to the deposition conditions of block SC, was deposited to extract plate-type tensile samples. Wire-electronic discharge machining (W-EDM) was used for machining the tensile samples. Samples
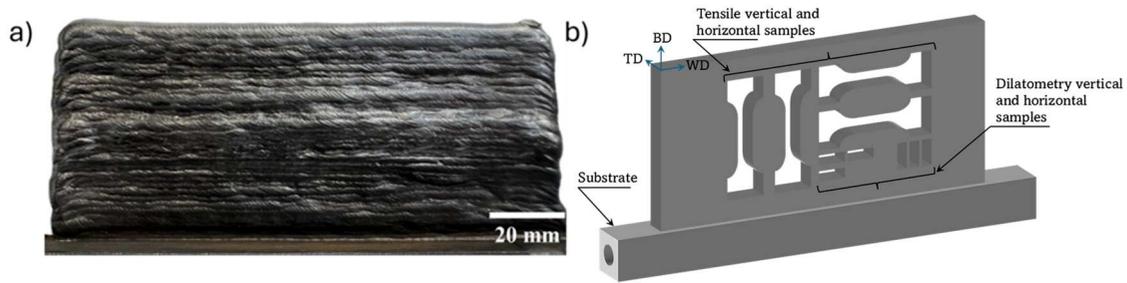
Figure 2. overview of the as-deposited SDM block in (a), and the schematic of the block after extracting tensile and dilatometry samples in (b). BD, WD and TD refer to the building, welding and transverse directions, respectively.

oriented parallel to the building (four samples) and welding (four samples) directions were extracted to quantify the tensile properties in two directions of the block. The sample geometry and testing procedure were based on the guidelines stated in the ISO 6892-19 standard [32]. The tensile tests were performed at room temperature with an INSTRON® 5500R machine at a displacement rate of 1 mm min^{-1} using a contact extensometer. The as-deposited block is shown in Figure 2(a), and the sample extraction is schematically illustrated in Figure 2(b).

Thermal expansion analysis

Cylindrical specimens of Φ 4 mm × 10 mm were extracted from block SDM using W-EDM for dilatometric analysis, as shown in Figure 2(b). A Linseis TMA PT1000 thermomechanical analyser was used for evaluating the linear coefficient of thermal expansion (CTE) of the as-deposited LTE36 alloy containing TiC particles. The temperature-displacement (T-D) curves were measured for two sets of samples: the first set, oriented along the building direction (three samples), and the second set, oriented along the welding direction (three samples), to establish the properties in two directions. The measurements were performed following the guidelines of the ASTM E831-19 standard [33]. The T-D curves were measured between room temperature (RT) and 550 °C at a heating rate of 5 °C min^{-1} in an inert environment with argon gas. The CTEs were calculated from the T-D curves by equation (1):

$$\alpha = \frac{1}{L_0}\frac{dL}{dT},$$ (1)

where, α is the mean CTE to desired temperature interval; L_0 is the initial length of the specimen; dL is the change in length of the specimen accompanied by the temperature variation; dT is the temperature variation. Samples for tensile testing and dilatometric measurements were extracted from the bulk of the

SDM block, ensuring microstructural similarity among the samples.

Results and discussion

Thermal history and melt pool observations

The time-temperature curves during the deposition of LTE36 alloy for the cases when external cooling was off (reference) and on are shown in Figure 3(a): (a-0) and (a-1), respectively. An approximately constant inter-pass (T_I) temperature of 70 °C was maintained between successive passes for both cases as marked in the figures. For the reference case, the time taken to deposit five beads was approximately 2100 s. In comparison, when accelerated cooling was used the time taken to deposit five beads reduced to approximately 650 s (70% reduction). The accumulation of heat due to successive passes was also evident during the deposition without the use of accelerated cooling. The times t_1 to t_4 indicate the inter-pass times in figure (a-0) and are also applicable to figure (a-1). These inter-pass times are ordered as follows: $t_1 < t_2 < t_3 < t_4$ in the reference/no cooling case, and $t_1 < t_2 \approx t_3 \approx t_4$ in the accelerated cooling case. The accumulation of heat during WAAM of LTE36 alloy can be attributed to the relatively low thermal diffusivity of the alloy [34].

Melt pool observations were performed to establish the effect of cooling on the melt pool characteristics using a specialised welding camera. The observed melt pool for the deposition cases of reference and accelerated cooling is shown in Figure 3 (b): (b-0) and (b-1), respectively. The length of the melt pool in the two deposition cases was also measured and is listed in Figure 3(b). The length of the melt pool in the reference case at $t = 11$ s during the deposition was measured as 18.8 mm. At a similar time, i.e. 13 s, during the deposition case with accelerated cooling the melt pool length is measured as 15.3 mm. Due to the build-up of heat, the melt pool in the reference case is more elongated than in the case of external cooling. The elongation is
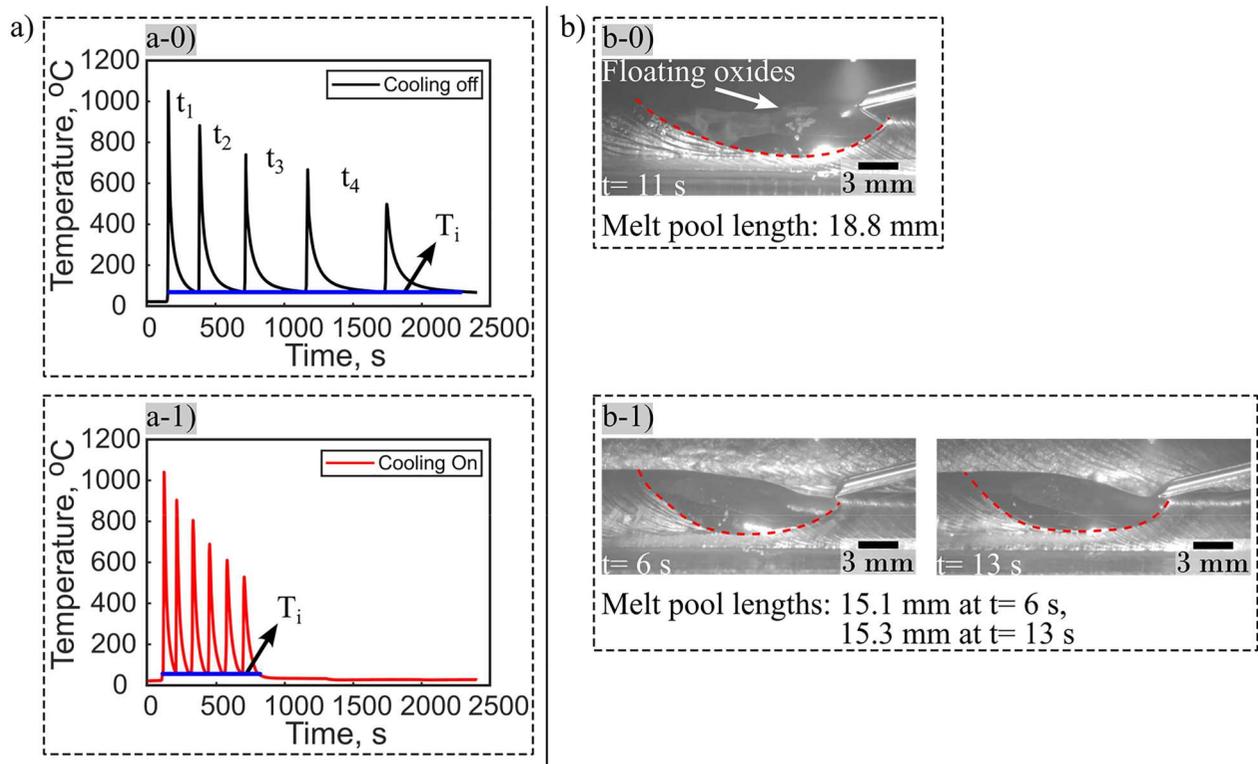
Figure 3. time-temperature curves obtained during the deposition of LTE36 alloy without and with accelerated cooling by a CO_2 jet in (a): (a-0) and (a-1), respectively, and the observed melt pool corresponding to the deposition conditions of (a), in (b).

promoted when the rate of latent heat release upon solidification at the melt pool's tail along the centreline exceeds the heat dissipation rate [35]. The application of a CO_2 jet to the substrate effectively dissipates heat by imposing a heat sink effect on the substrate, thereby preventing the elongation of the melt pool. Furthermore, the strategy of forced cooling through the substrate ensures a homogeneous cooling effect throughout the deposition process, as the cooling jet remains active until the desired inter-pass temperature (~ 70 °C in this study) is achieved. The uniform cooling effect provided by the jet is evident in the relatively consistent length of the melt pool towards the start ($t = 6$ s) and end ($t = 13$ s) of the deposition case with accelerated cooling, as shown in Figure 3(b-1).

Large oxide islands floating on the melt pool were also observed for the reference case, as shown in Figure 3(b-0). These oxides are likely to form in the reference case due to a lack of appropriate shielding arising from the elongation of the melt pool. On solidification of the melt pool, these oxides appear on the deposited beads and negatively affect the surface quality, thus increasing the risk of lack of fusion defects unless properly cleaned. Management of the heat using accelerated cooling also affected the macroscopic deposition quality of LTE36 alloy. The larger SDM block deposited in this study, as shown in Figure 2(a),

did not experience a tapering of its ends compared to a similar block deposited in our earlier work. Despite the uni-directional deposition, the block deposited in this study exhibits better geometrical stability due to the prevention of heat accumulation. Overall, the net effect of cooling is to promote heat extraction during the WAAM process. This, in turn, is expected to reduce the tendency of grain coarsening during the deposition of single-phase LTE36 alloy at a microstructural level.

Microstructure and phase analysis

The microstructures of the LTE36 alloy in various deposition conditions are presented in Figure 4. Severe grain coarsening is observed in the reference case (SR), which led to the formation of intergranular cracks. An example of this is shown in Figure 4(a), where the crack is observed to form at the triple point of the coarsened grains. SEM observations of the crack flank reveal a wavy appearance, and some isolated instances of micro-dimples (Figure 4(a-0)), thus suggesting limited ductility. The intergranular nature of the crack at the triple junction of coarsened grains, combined with the characteristic morphology of the crack flank, confirms that the observed cracking is associated with the phenomenon of ductility-dip cracking (DDC). These
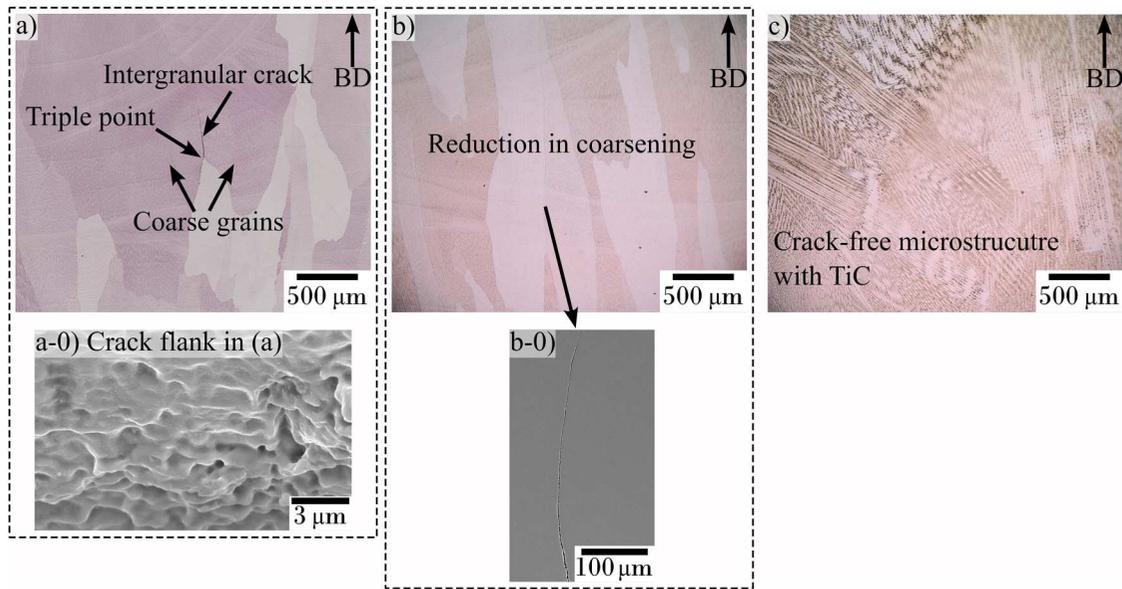
Figure 4. microstructure of block SR showing coarsened grains and an intergranular crack in (a). Reduction in the extent of grain coarsening though accelerated cooling during the deposition of block SCL shown by the micrograph in (b), and an intergranular crack in (b-0). Crack-free microstructure of LTE36 alloy achieved through the addition of TiC in (c), corresponding to a sample from block SC.

Table 2. Ti and C contents in the specimens of as-deposited blocks measured by XRD and LECO analysis, respectively.

| Sample, wt.%	SA	SB	SC
Ti (XRF)	0.33 ± 0.01	0.52 ± 0.03	0.71 ± 0.04
C (LECO)	0.08 ± 0.01	0.16 ± 0.01	0.24 ± 0.02

findings are consistent with the results reported in our previous work on WAAM of LTE36 alloy [26].

Accelerated CO_2 jet cooling was employed to prevent the coarsening of grains during the deposition of LTE36 alloy (block SCL), and the resulting microstructure is shown in Figure 4(b). At first glance, the cooling strategy appears effective in reducing grain coarsening, which in turn prevents the formation of large intergranular cracks, such as the one shown in Figure 4(a). However, SEM observations revealed the persistence of micro-cracks in the microstructure obtained after using the cooling jet, as depicted in Figure 4(b-0).

The cooling strategy was further combined with the interlayer application of TiC powder particles during WAAM of LTE36 alloy. The sample designations and chemical compositions are listed in Table 2, corresponding to the depositions with the combined approach of cooling and TiC powder particles. The microstructure of block SC was found to be free of cracks, as shown in Figure 4(c). Additionally, the microstructure of block SC appears refined than that of block SR. Detailed analyses of the microstructures in blocks SR, SCL, and SA to SC were performed using EBSD, the corresponding grain boundary maps are shown in Figure 5(a), (b), and (c) to

(e), respectively. Coarse columnar grains with non-tortuous grain boundaries are revealed in Figure 5(a). The extent of grain coarsening is reduced in block SCL (only cooling), as observed in Figure 5(b). The addition of TiC particles significantly modified the micro-structures in terms of grain boundary morphology and columnar grain widths. As the TiC content increases (blocks SA to SC), the grain boundaries develop tortuosity, accompanied by simultaneous reduction in columnar grain width, as listed in Table 3, which was calculated using the linear intercept method [36]. This can be qualitatively observed when comparing the grain boundary maps shown in Figure 5(a) to (e).

The grain boundary maps of blocks SB and SC also revealed the presence of stray equiaxed-like grains. This indicates that the TiC particles can act as a grain-refining inoculant during WAAM of LTE36 alloy by promoting heterogeneous nucleation. However, the limited occurrence of equiaxed-like grains in the micro-structures of blocks SB and SC suggests that the amount of TiC particles was likely insufficient to promote heterogeneous nucleation uniformly throughout the blocks. Future work can be undertaken to better understand the extent of heterogeneous nucleation in LTE36 alloy facilitated by TiC particles during WAAM. The presence of DDC micro-cracks, similar to the crack shown in Figure 4(b), were occasionally observed in the microstructures of blocks SA and SB. However, cracks were eliminated from block SC, which contained higher amounts of TiC than blocks SA and
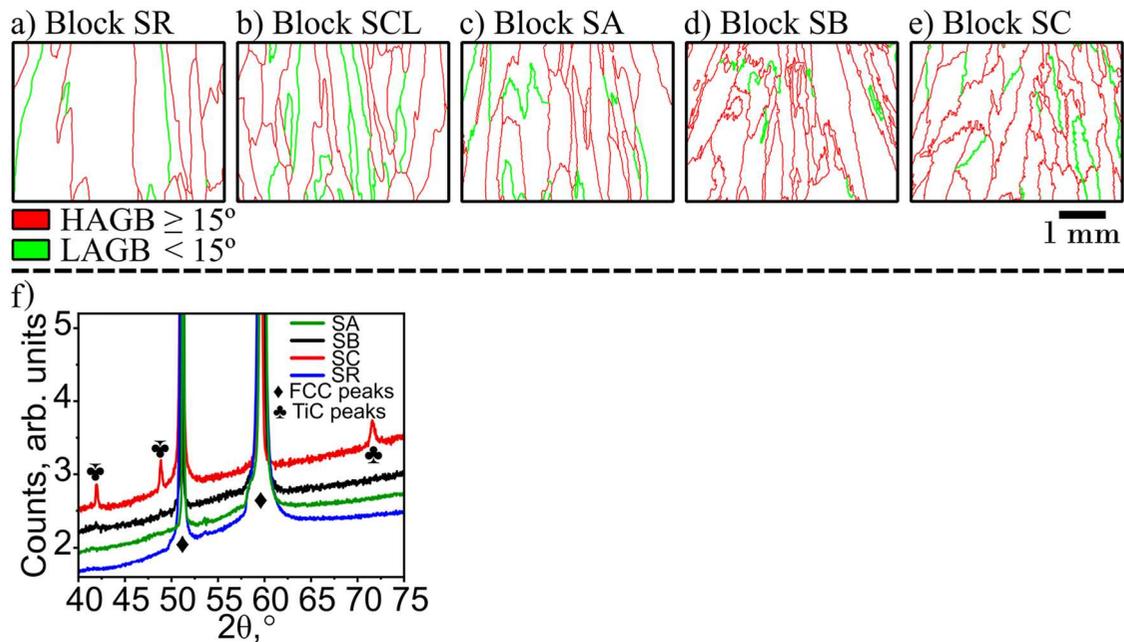
Figure 5. high (HAGB) and low angle (LAGB) grain boundary maps for samples of blocks SR, SCL, SA, SB, and SC in (a), (b), (c), (d), and (e), respectively. XRD patterns for samples of blocks SA, SB, SC, and SR revealing the detection of clear TiC peaks in the patterns corresponding to blocks SB and SC in (f).

Table 3. The average columnar grain widths quantified from the transverse cross-sections (BD-TD planes) of the deposited blocks using the linear intercept method. The cross-sections were taken at 25, 35, 45, and 55 mm from the start of the blocks.

Block	Average columnar grain width, μm
SR	1280 ± 260
SCL	760 ± 210
SA	510 ± 120
SB	470 ± 80
SC	380 ± 90

SB. This suggests that a minimum level of TiC addition was necessary to completely prevent cracking during WAAM of LTE36 alloy. Phase identification was conducted using XRD, and the resulting XRD patterns are presented in Figure 5(f). Clear TiC peaks were identified in the patterns of samples taken from blocks SC and SB, with the absence of these peaks in the pattern of the sample taken from block SA. However, the peak intensities corresponding to the TiC phase were reduced in the pattern of block SB compared to block SC. The TiC phase fractions were quantified as 0.3% and 0.7% by weight, with an error of ± 0.2%, in blocks SB and SC, respectively.

The microstructure of block SC was further anlaysed with a low-step size setting during EBSD to investigate the introduction of TiC particles. The grain maps, phase maps, and simultaneous EBSD-EDS map scans for block SC, are shown in Figure 6. In general, the grain boundaries (GBs) were decorated with faceted

and irregularly shaped particles, as shown in Figure 6. Most of these particles were observed to be sub-micron sized, with a few instances of particles ranging from sub-micron to micron-sized. Similarly, the grain interiors also exhibited the presence of such particles (Intragranular TiC in Figure 6). An example of a nano-sized particle within a grain of block SC can be seen in Figure 6 (Nano-TiC). The corresponding EDS maps in Figure 6 show enrichment of Ti, thus providing positive confirmation of TiC particles. The tortuosity in the GBs arises from the presence of the TiC particles. Consequently, the tortuous GBs restrict grain growth, thereby increasing the resistance to DDC compared to the non-tortuous GBs of block SR [37,38]. Altogether, these particles contribute to the clear TiC peaks in the XRD pattern of block SC, as shown earlier in Figure 5(f). In comparison, the reduced peak intensity and the absence of TiC peaks in the XRD patterns of blocks SB and SA can be attributed to the limited presence of nano-TiC particles. An example of such nano-TiC particles observed in the microstructure of block SB is shown in Figure 7.

The mechanisms responsible for the reduced susceptibility of LTE36 alloy to intergranular DDC due to accelerated cooling and TiC addition are schematically shown in Figure 8. During WAAM of LTE36 alloy, heat accumulation may occur due to the relatively low thermal diffusivity of the alloy [34]. This, along with the alloy's persistence in the single-phase austenitic
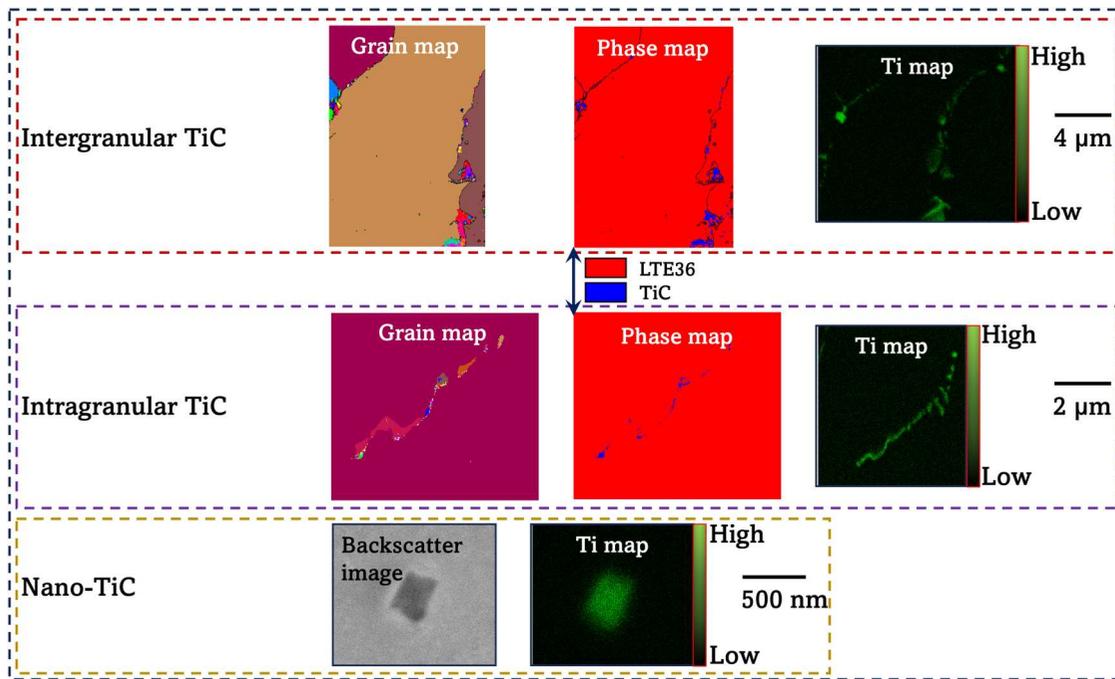
Figure 6. morphology of the TiC particles in the microstructure of a sample taken from block SC.
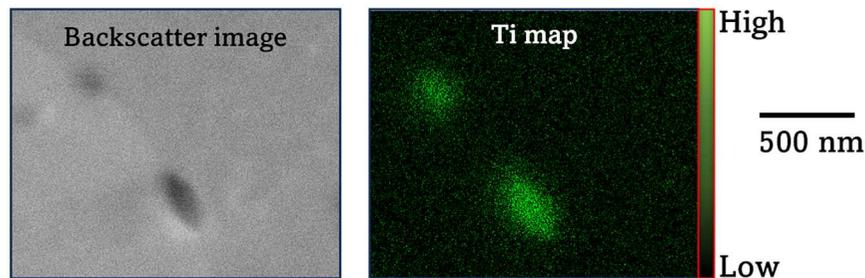

Figure 7. chemical analysis of the nano-particles observed in the microstructure of a sample taken from block SB.

structure, up to its liquidus temperature, promotes a microstructure conducive to grain coarsening. The propensity for grain coarsening arises from the low activation energy of grain growth in LTE36 alloy (Invar), and a system's tendency to minimise free energy through boundary migration [34,39]. Therefore, grain coarsening occurs during the WAAM process, as schematically illustrated in Figure 8(a), leading to a net reduction in total GB area.

Furthermore, WAAM inherently induces non-uniform thermal stresses/strains, which the deposited material accommodates [40]. The reduction in GB area due to abnormal grain coarsening during WAAM increases the stress/strain accommodated per GB. When the localised stress or strain surpasses the GB strength, intergranular DDC occurs, as shown schematically in Figure 8(a).

A cooling system, such as the CO_2 jet utilised in this study, facilitates heat extraction from the LTE36 alloy

during WAAM, thereby limiting grain coarsening, as illustrated in Figure 8(b). The cooling jet mitigates heat accumulation by effectively transforming the substrate into a heat sink. Hence, the thermal energy available for GB migration and the duration for which material remains at elevated temperatures are reduced. This promotes the retention of a greater GB area compared to the condition in Figure 8(a), where accelerated cooling is not applied. Consequently, the extent of DDC is reduced, with GBs exhibiting smaller and thinner cracks or micro-cracks, as observed in Figure 8(b), in contrast to the larger crack shown in Figure 8(a). The persistence of micro-cracks despite utilising accelerated cooling can be attributed to the overall cooling effect on the deposited material rather than a more targeted local cooling approach, such as directing the cooling jet behind the melt pool. Additionally, the microstructure of LTE36 alloy deposited with accelerated cooling
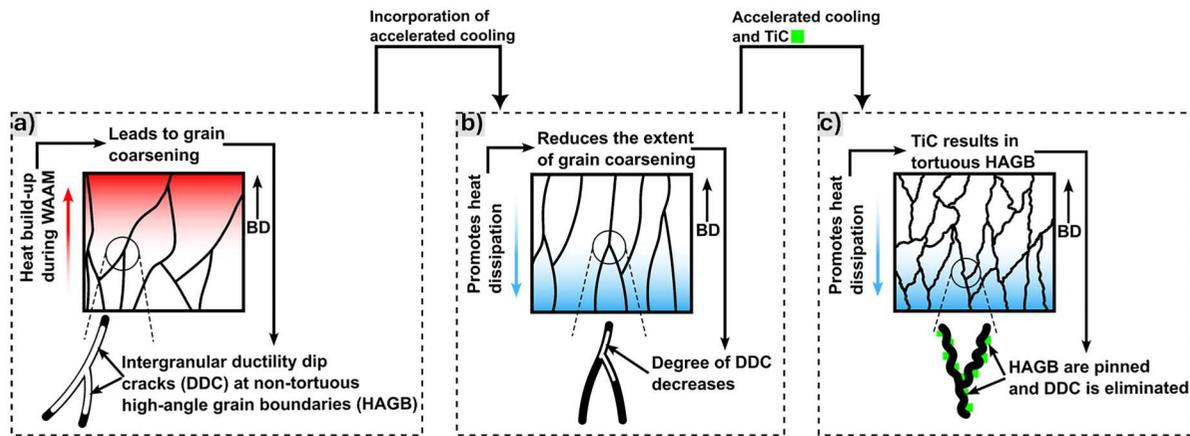
Figure 8. schematic illustration of the microstructure development in LTE36 alloy during WAAM in (a), by incorporating accelerated cooling in (b), and a combination of accelerated cooling and TiC particles in (c).

exhibits non-tortuous GBs, similar to those depicted in Figure 8(a), which are inherently susceptible to DDC [37].

Naturally, alleviating DDC from LTE36 alloy during WAAM necessitates the modification of the GB morphology [41, 42]. This can be achieved by introducing TiC particles, as shown in Figure 8(c). The presence of TiC particles in the melt pool allows for effective pinning of the GBs, thereby restricting their migration. This restriction on GB movement further reduces grain coarsening, leading to a decrease in columnar grain widths with increasing TiC content, as observed in blocks SA to SC. Additionally, the presence of equiaxed-like grains, similar to those observed in the microstructures of blocks SB and SC, contributes in increasing the GB area. The restriction on the migration of GBs due to the presence of TiC particles helps retain their zig-zag tortuous morphology. This tortuosity of the GBs may also provide a mechanical interlocking effect between adjacent grains. Consequently, in block SC, the GBs of LTE36 alloy transition from crack-susceptible to crack-resistant upon the introduction of TiC particles.

In summary, the microstructure of the as-deposited LTE36 alloy consists of columnar grains aligned along the building direction. However, these grains are susceptible to severe coarsening due to heat build-up during the deposition process, as observed in the microstructure of the reference (SR) sample. This coarsening can be mitigated by employing an external cooling strategy during deposition, such as the CO_2 jet used in this study, which effectively promotes heat dissipation. The accelerated cooling strategy also reduces the extent of DDC in the LTE36 alloy due to its influence on the microstructure. Nevertheless, the combined approach of cooling and the incorporation of TiC powder particles was necessary to eliminate DDC in LTE36 alloy. This indicates that the cooling strategy alone, as applied in this study, was insufficient to completely prevent DDC. An improvement of the cooling strategy could involve the development of a setup utilising a specialised nozzle capable of delivering a cooling medium trailing the arc. Future studies employing this setup during the deposition of LTE36 alloy are recommended, as this work demonstrates noticeable enhancement in both the microstructure and interpass times of the LTE36 alloy deposited with accelerated cooling. Additionally, the use of accelerated cooling may also have been beneficial in lowering the minimum amount of TiC required to eliminate DDC. Without cooling, it is highly likely that the LTE36 alloy would remain prone to grain coarsening until higher amounts of TiC than those used in block SC are incorporated, due to the heat accumulation effects during WAAM. Ductility-dip cracking is a GB phenomenon, characterised by the failure of GBs due to their reduced ductility at elevated temperatures under the influence of stress/strain [43]. In general, single-phase fcc alloys, such as LTE36, are prone to DDC because of a loss of GB ductility at elevated temperatures [44,45]. Processing the LTE36 alloy by WAAM subjects the material to the ideal conditions for DDC, namely elevated temperatures caused by molten metal deposition and the generation of process-induced stresses/strains. During WAAM of LTE36 alloy, the addition of TiC particles effectively pins the GBs and induces tortuosity, thereby resisting grain coarsening. These combined effects, resulting from the presence of TiC particles at the GBs, promote a crack-free microstructure by reducing the susceptibility of the LTE36 alloy to DDC.

Functional properties

The engineering stress-strain curves obtained from the tensile tests performed on samples from block SDM
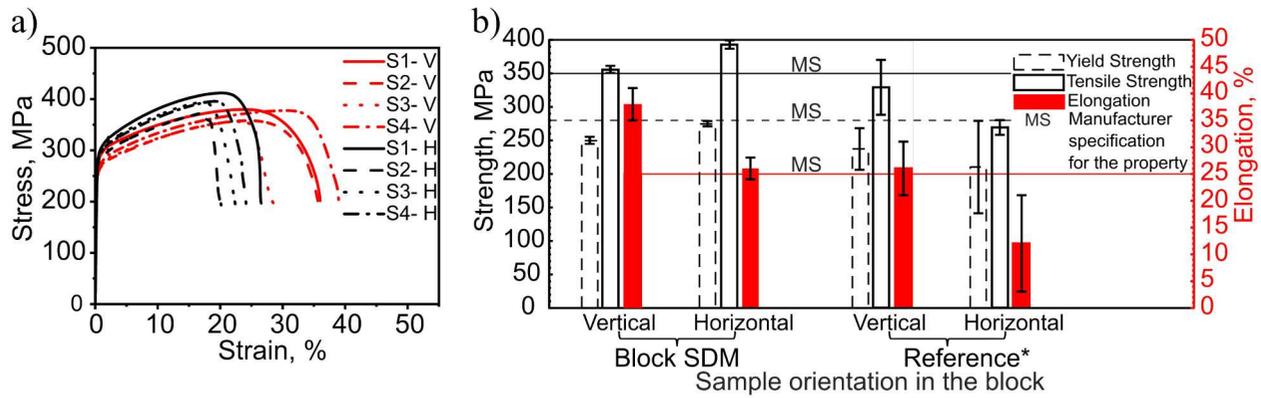
Figure 9. measured strain-strain curves of the specimens extracted from block SDM oriented along the building (V) and welding (H) directions in (a). Tensile properties calculated from the curves in (a), shown in (b). *: The poor tensile properties for reference in (b) due to the presence of intergranular cracks are adapted from an earlier work on WAAM of LTE36 alloy [26].

are shown in Figure 9(a). The properties were evaluated along two directions of the block to quantify any directional anisotropy. This is represented by the results of samples oriented in the horizontal (H, WD) and the vertical (V, BD) directions. As shown in Figure 9(b), the mechanical properties of block SDM are in good agreement with the expected values (MS), regardless of the orientation. This agreement is attributed to the absence of DDC in block SDM. The tensile properties corresponding to the reference in Figure 9(b) are adapted from our earlier work to highlight the detrimental effect of DDC on the mechanical performance of as-deposited LTE36 alloy [26]. Intergranular ductility-dip cracks act as stress concentrators or sites for preferential damage, leading to premature failure of LTE36 alloy under tensile loading. Conversely, the addition of TiC increases the resistance of the grain boundaries to DDC by inducing tortuosity, effectively pinning them and preventing crack formation. Hence, DDC during

WAAM of LTE36 alloy is mitigated by the combined approach of accelerated cooling and the addition of TiC particles, thereby recovering or exceeding the expected mechanical properties of the LTE36 alloy. However, the mechanical properties exhibit orientation-dependent anisotropic behaviour. The horizontally oriented specimens are found to be stronger and less ductile compared to vertically oriented specimens. This strength-ductility anisotropy between the horizontally and vertically oriented specimens can be related to the strong directionality of the columnar grains. The vertical specimens are extracted with their length oriented along the building direction of block SDM, which aligns the specimen length with the long axis of the columnar grains. Due to this alignment, the grain boundary density in the vertical specimens is reduced relative to the horizontal specimens. Consequently, the hindrance to dislocation slip by grain boundaries is lower in vertical specimens than in horizontal
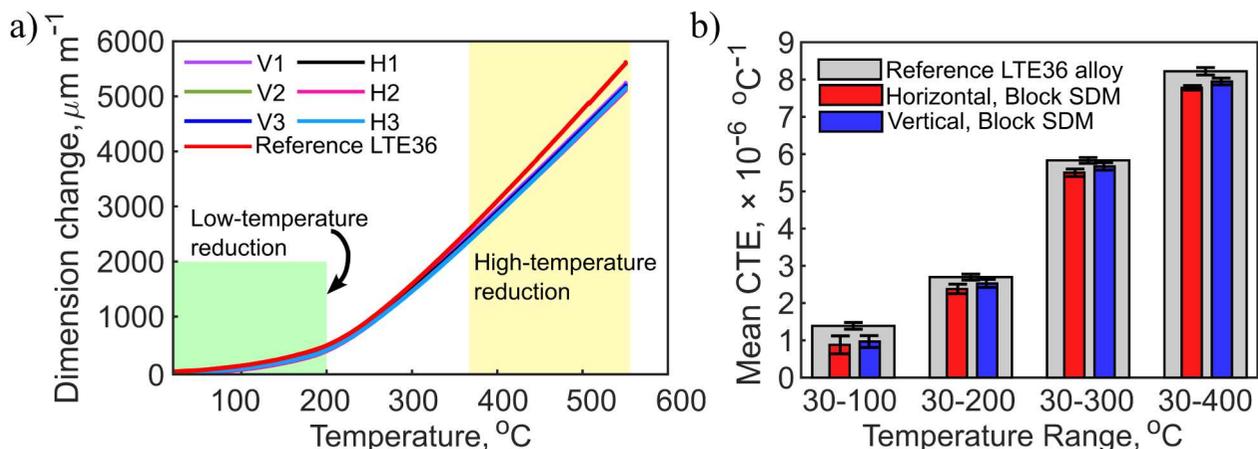
Figure 10. temperature-displacement curves of the specimens extracted from block SDM oriented along the building (V) and welding (H) directions in (a). Mean CTEs in various temperature ranges calculated from the T-D curves in (a), shown in (b).

specimens. This results in the conflicting behaviour of strength and ductility between the horizontally and vertically oriented specimens. A similar trend has also been observed in other studies addressing the mechanical properties of S304L steel and LTE36 alloy fabricated by WAAM [15,46].

The measured temperature-displacement (T-D) curves of specimens from block SDM are shown in Figure 10(a). For comparison, an averaged T-D curve of two samples from SR block (without cooling or TiC addition) is also added to the figure. The mean linear coefficients of thermal expansion (CTEs) in different temperature ranges were calculated from these curves and are presented in Figure 10(b). No significant anisotropy is observed between the CTEs of specimens oriented vertically and horizontally within the block. However, a noticeable reduction in the CTEs of specimens from block SDM is observed when compared to the CTEs of the reference LTE36 alloy (block SR). This reduction of CTE is highlighted in two parts in Figure 10(a). Firstly, a prominent low-temperature reduction in the thermal expansion behaviour of block SDM is revealed in the low-temperature range of 30–100 °C, i.e. well below the Curie transition. Secondly, a high-temperature reduction of the thermal expansion behaviour occurs upon exceeding the ferromagnetic ordering temperature (Curie transition). This high-temperature reduction can be attributed to the composite nature of the LTE36 alloy comprising TiC particles. The mean linear CTE of TiC particles, reported to be approximately 6.99 $\mu m\ m^{-1}\ °C^{-1}$ in a temperature range of 30–500 °C, is lower than that of the reference LTE36 alloy in the same range, which is 10.10 $\mu m\ m^{-1}\ °C^{-1}$, as determined from Figure 10(a) [47]. The crossover between the mean CTE

of the reference LTE36 alloy and TiC particles, determined from room temperature, occurs at around 300 °C; above this temperature, the CTE of TiC particles is lower than that of the reference LTE36 alloy. The deposited LTE36 alloy comprising TiC particles can be considered a metal matrix composite. For such materials, the net thermal expansion is typically estimated using a rule-of-mixtures approximation. Hence, the lower CTE of TiC particles compared to that of the reference LTE36 alloy above temperatures of 300 °C leads to a high-temperature reduction of the thermal expansion behaviour in LTE36 alloy comprising TiC particles (block SDM) relative to the reference LTE36 (block SR) alloy.

However, it should be noted that this high-temperature reduction holds little significance for the aerospace mould tooling applications of LTE36 alloy. This is because these tools are typically limited to a maximum operational temperature of 200 °C during composite curing cycles [48].

Based on the above reasoning for the high-temperature reduction, it can also be argued that the mean linear CTE of LTE36 alloy comprising TiC particles in the temperature range of 30–100 °C should increase compared to that of the reference LTE36 alloy. Since for temperatures below 300 °C, the CTE of TiC particles is higher than that of the reference LTE36 alloy. Moreover, the CTEs of LTE36 alloy in various temperature ranges are expected to increase with the addition of Ti and C, provided these elements are present in the solid-solution matrix. However, the addition of TiC particles to the LTE36 alloy in this study contributes marginally to the chemical composition of the solid-solution matrix. This is valid based on the low solubility product of TiC in austenite (0.0165 at 1200 °C), indicating that these particles
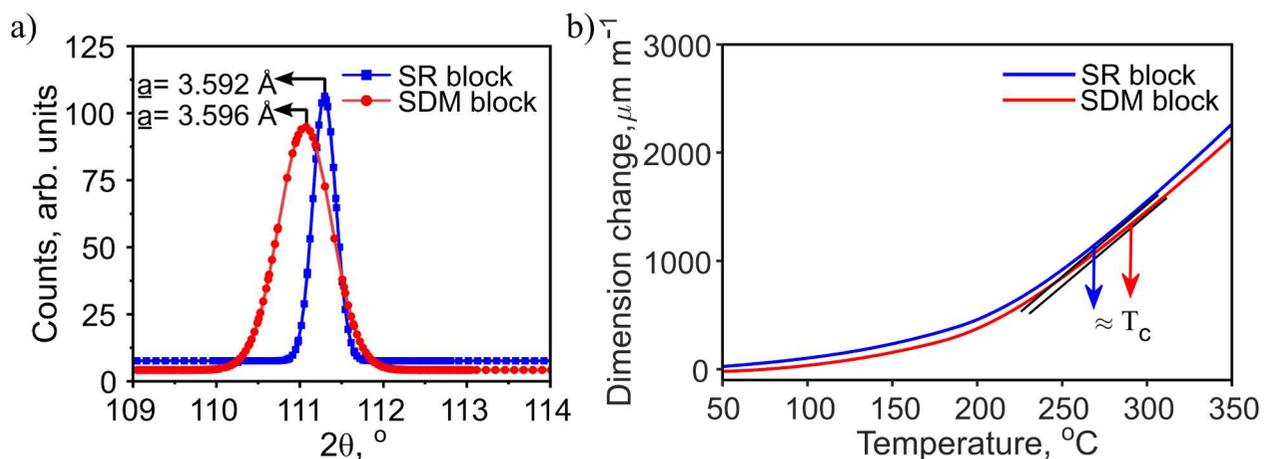
Figure 11. lattice parameters obtained from the XRD patterns of specimens from blocks SR and SDM in (a), symbols correspond to the measured points to which the solid lines are fitted. Approximation of the Curie temperatures from the average T-D curves of samples from blocks SDM and SR.

remain stable with limited dissolution at high temperatures in the austenitic matrix of the LTE36 alloy [49]. Consequently, the low thermal expansion behaviour of LTE36 alloy should be minimally influenced by TiC from the perspective of chemically induced changes. However, due to the repetitive thermal cycles in WAAM, some degree of dissolution can be expected, which in turn could result in a marginal yet observable increase in the CTE of LTE36 alloy. For instance, the change in the CTE of FeNi36 alloy per mass% of Ti addition in the temperature range of 30–100 °C is reported to be approximately 0.86 µm m^{-1} °C^{-1} [50]. Hence, contrary to the expected increase in the same temperature range, a low-temperature reduction is observed in the thermal expansion behaviour of LTE36 alloy comprising TiC particles compared to that of the reference LTE36 alloy, as highlighted in Figure 10(a). This manifests as a prominent reduction in the mean linear CTE of block SDM evaluated in the temperature range of 30–100 °C relative to that of block SR, as shown in Figure 10(b).

To understand the observed low-temperature reduction of CTE in this work, the effect of TiC addition on the lattice parameter of the deposited specimens was explored. The high-angle XRD diffraction peaks corresponding to specimens of blocks SR and SDM are shown in Figure 11(a). The values of the lattice parameters (a), listed in Figure 11(a), were calculated using the corresponding Nelson-Riley extrapolation plots [51]. From Figure 11(a), it is evident that the addition of TiC resulted in an increase in the a value, which reveals as a shift in the XRD peak positions. This suggests that the marginal increase in a value is linked to the reduction in the CTEs observed in this study. The relationship between increasing a value and reduction in the CTE of LTE36 alloy can be explained based on the simultaneous improvement in magnetic exchange coupling. The magnetic exchange coupling (exchange interaction) is fundamental in the description of ferromagnetism [52, 53]. The increase in a value is expected to influence the Fe-Fe exchange interaction such that its ferromagnetic character is enhanced. This argument is supported by the computational work of Rancourt et al. that addressed the physical phenomenon underlying the low thermal expansion behaviour of Invar 36 [54]. Using local moment models, they demonstrated that the Fe-Fe magnetic exchange bonds in Invar 36 improve their ferromagnetic character as the interatomic separation increases. In addition to the computational work, Gorria et al. provided experimental evidence using X-ray absorption spectroscopy, suggesting that mechanical stressing of Invar 36 primarily affects the Fe–Fe interatomic distances [55]. An increase in these distances was found to favour ferromagnetism.

The calculation of the magnetic exchange integral terms is beyond the scope of this article. However, an estimate about the trend of the exchange integral can be made through the relationship between the ferromagnetic Curie temperature and the exchange integral, as described by the mean field theory in equation (2):

$$T_c = \frac{J_{ex}Z_T S(S+1)}{3k_B},\qquad(2)$$

where, T_c is the Curie Temperature, Z_T is the co-ordination number, S is the atomic spin quantum number, J_{ex} is the exchange integral, and k_B is the Boltzmann constant [56]. The Curie temperature and the exchange integral are directly proportional for a constant value of the other parameters, which is the case in this study. Therefore, T_c would only increase if the exchange integral, J_{ex} increases. The Curie temperature for the SDM block is observed to be lower than that of block SR, as illustrated by the averaged T-D curves shown in Figure 11(b). This implies that the difference in the T_c between blocks SDM and SR results from the higher exchange integral, which arises from an increase in a value due to the addition of TiC in block SDM. The synergy between the lattice parameter and magnetic exchange interaction also supports the observed prominent reduction of the CTE in the low-temperature range, well below the Curie transition. Therefore, the increment in the lattice parameter of LTE36 alloy enhances its ferromagnetic character and, consequently, its low thermal expansion behaviour. This leads to a prominent reduction in the CTE at temperatures well below the Curie transition, as observed in this study.

Conclusions

In this work, we systematically studied the microstructural and functional response of LTE36 alloy to accelerated cooling and TiC particle addition during WAAM. The combined approach led to the defect-free fabrication of the alloy with improved functional performance. The outcomes of this study are concluded as follows:

1. Employing accelerated cooling during wire arc additive manufacturing (WAAM) of the single-phase LTE36 alloy reduces the susceptibility to ductility-dip cracking (DDC) and shortens the interpass times. However, the elimination of DDC requires the addition of TiC particles.
2. The microstructure of the LTE36 alloy is refined through the addition of TiC particles, which reduces the extent of grain coarsening during WAAM. The degree of grain coarsening decreases as the TiC

content increases, effectively promoting the pinning of high-angle grain boundaries (HAGBs). The TiC particles also induce tortuosity at the HAGBs. This morphological change further contributes to lowering the susceptibility to DDC.

3. The tensile properties of LTE36 alloy containing TiC particles are significantly improved compared to the TiC-free alloy, which exhibits DDC. The average tensile strength, yield strength, and elongation increase by 24%, 18%, and 60%, respectively.

4. The tensile properties of LTE36 alloy processed with the combined approach of accelerated cooling and TiC particle addition are anisotropic with respect to the building and travel directions. This anisotropy arises from the alignment of the columnar grains along the building direction.

5. The mean CTE of the LTE36 alloy comprising TiC particles in the temperature range of 30–100 °C is lower than that of the TiC-free alloy. This reduction is attributed to the lattice parameter increase observed in the TiC-containing alloy, which enhances the ferromagnetic character of the alloy.

Acknowledgements

Disclosure statement

No potential conflict of interest was reported by the author(s).

Funding

Data availability statement

The data that support the findings of this study are available from the corresponding author, A. Sood, upon reasonable request.

ORCID

Arjun Sood http://orcid.org/0000-0002-4193-7516
Constantinos Goulas http://orcid.org/0000-0003-4910-1761
Vera Popovich http://orcid.org/0000-0002-3513-3378
Marcel J. M. Hermans http://orcid.org/0000-0002-6204-5285

References

[1] Phagare M. Nickel Alloy Market Report 2024 (Global Edition), 8th ed. 2024. Accessed: Sep. 12, 2024. [Online]. Available: https://www.cognitivemarketresearch.com/nickel-alloy-market-report.

[2] Huang G, He G, Gong X, et al. Additive manufacturing of Invar 36 alloy. J Mater Res Technol. 2024;30:1241–1268. doi:10.1016/j.jmrt.2024.02.221

[3] Sood A, Schimmel J, Bosman M, et al. Fabrication of low thermal expansion Fe–Ni alloys by in-situ alloying using twin-wire arc additive manufacturing. Mater Des. 2024;240:1241–1268. doi:10.1016/j.matdes.2024.112837

[4] Sahoo A, Medicherla VRR. Fe-Ni invar alloys: a review. Mater Today Procs. 2021;43:2242–2244.

[5] Shah DB, Patel KM, Patel AI, et al. Experimental investigation on spring-back deformation during autoclave curing of parabolic antenna reflectors. Compos Part A Appl Sci Manuf. 2018;115:134–146. doi:10.1016/j.compositesa.2018.09.017

[6] Khanna N, Srivastava A. Optimization and analysis of surface roughness for INVAR-36 in end milling operations. 2018. [Online]. Available: www.sciencedirect.comwww.materialstoday.com/proceedings2214-7853.

[7] Abbasi SM, Morakabati M, Mahdavi R, et al. Effect of microalloying additions on the hot ductility of cast FeNi36. J Alloys Compd. 2015;639:602–610. doi:10.1016/j.jallcom.2015.03.167

[8] Williams SW, Martina F, Addison AC, et al. Wire + Arc additive manufacturing. Mat Sci Technol. 2016;32(7):641–647. doi:10.1179/1743284715Y.0000000073

[9] Li K, Yang T, Gong N, et al. Additive manufacturing of ultra-high strength steels: A review. Nov. 25, 2023, Elsevier Ltd. doi:10.1016/j.jallcom.2023.171390.

[10] Jafari D, Vaneker THJ, Gibson I. Wire and arc additive manufacturing: Opportunities and challenges to control the quality and accuracy of manufactured parts. Mater Des. 2021;202:109471. doi:10.1016/j.matdes.2021.109471

[11] Li Y, Su C, Zhu J. Comprehensive review of wire arc additive manufacturing: Hardware system, physical process, monitoring, property characterization, application and future prospects. Mar. 01, 2022, Elsevier B.V. doi:10.1016/j.rineng.2021.100330

[12] Pattanayak S, Sahoo SK. Gas metal arc welding based additive manufacturing—a review. 2021, Elsevier Ltd. doi:10.1016/j.cirpj.2021.04.010

[13] Veiga F, Suarez A, Aldalur E, et al. Wire arc additive manufacturing of invar parts: Bead geometry and melt pool monitoring. Measurement. 2022;189:110452. doi:10.1016/j.measurement.2021.110452

[14] Gil Del Val A, Cearsolo X, Suarez A, et al. Machinability characterization in end milling of Invar 36 fabricated by wire arc additive manufacturing. J Mater Res Technol. 2023;23:300–315. doi:10.1016/j.jmrt.2022.12.182

[15] Veiga F, Suárez A, Artaza T, et al. Effect of the heat input on wire-arc additive manufacturing of Invar 36 alloy: microstructure and mechanical properties. Weld World. 2022;66(6):1081–1091. doi:10.1007/s40194-022-01295-4

[16] Aldalur E, Suárez A, Veiga F. Thermal expansion behaviour of Invar 36 alloy parts fabricated by wire-arc additive manufacturing. J Mater Res Technol. 2022;19:3634–3645. doi:10.1016/j.jmrt.2022.06.114

[17] Jiao G, Fang X, Li X, et al. High performance ultrasonic vibration assisted Wire-arc directed energy deposition of Invar alloy. J Mater Process Technol. 2024;332:118534. doi:10.1016/j.jmatprotec.2024.118534

[18] Jiao G, Fang X, Chen X, et al. The origin of low thermal expansion coefficient and enhanced tensile properties of Invar alloy fabricated by directed energy deposition. J Mater Process Technol. 2023;317:117994. doi:10.1016/j.jmatprotec.2023.117994

[19] Wang J, Biswal R, Chen G, et al. On the composition gradient of steel/Invar functionally graded material manufactured by wire-based direct energy deposition. Addit Manuf. 2024;96:104594. doi:10.1016/j.addma.2024.104594

[20] Iturrioz A, Ukar E, Pereira JC. Influence of the manufacturing strategy on the microstructure and mechanical properties of Invar 36 alloy parts manufactured by CMT-WAAM. Int J Adv Manuf Technol. 2024;136:729–744.. doi:10.1007/s00170-024-14853-5

[21] Jiao G, Fang X, Zhang M, et al. Synergistic improvement of mechanical property and thermal expansion of Wire-arc DED Invar alloy enabled by a novel deposition strategy. J Manuf Process. 2024;121:121–135. doi:10.1016/j.jmapro.2024.05.031

[22] Wegener T, Pramanik S, Niendorf T, et al. On the cyclic deformation behavior of wire-based directed energy deposited Fe-Ni Invar alloy. Mater Sci Eng A. 2024;918:147403. doi:10.1016/j.msea.2024.147403

[23] Fernández-Zabalza A, Veiga F, Suárez A, et al. The use of virtual sensors for bead size measurements in wire-arc directed energy deposition. Appl Sci. 2024;14(5):1972. doi:10.3390/app14051972

[24] Qiu C, Adkins NJE, Attallah MM. Selective laser melting of Invar 36: microstructure and properties. Acta Mater. 2016;103:382–395. doi:10.1016/j.actamat.2015.10.020

[25] Tan H, Wang Y, Wang G, et al. Investigation on microstructure and properties of laser solid formed low expansion Invar 36 alloy. J Mater Res Technol. 2020;9(3):5827–5839. doi:10.1016/j.jmrt.2020.03.108

[26] Sood A, Schimmel J, Ferreira VM, et al. Directed energy deposition of Invar 36 alloy using cold wire pulsed gas tungsten arc welding: effect of heat input on the microstructure and functional behaviour. J Mater Res Technol. 2023;25:6183–6197. doi:10.1016/j.jmrt.2023.06.280

[27] Zhai W, Zhou W, Nai SML. Grain refinement and strengthening of 316L stainless steel through addition of TiC nanoparticles and selective laser melting. Mater Sci Eng A. 2022;832:142460. doi:10.1016/j.msea.2021.142460

[28] Koppu AK, Lautre NK, Motwani A, et al. Mechanical and microstructure investigation of TiC-inoculated SS316LSi thin wall deposited by CMT-WAAM. Trans Indian Inst Met. 2023;76(8):2307–2314. doi:10.1007/s12666-023-02943-z

[29] Zhai W, Zhu Z, Zhou W, et al. Selective laser melting of dispersed TiC particles strengthened 316L stainless steel. Compos B Eng. 2020;199:108291. doi:10.1016/j.compositesb.2020.108291

[30] Kennedy JR, Davis AE, Caballero AE, et al. The potential for grain refinement of Wire-Arc Additive Manufactured (WAAM) Ti-6Al-4 V by ZrN and TiN inoculation. Addit Manuf. 2021;40:1–11. doi:10.1016/j.addma.2021.101928

[31] Bermingham MJ, McDonald SD, Dargusch MS. Effect of trace lanthanum hexaboride and boron additions on microstructure, tensile properties and anisotropy of Ti-6Al-4 V produced by additive manufacturing. Mater Sci Eng A. 2018;719:1–11. doi:10.1016/j.msea.2018.02.012

[32] ISO standards. Metallic materials-Tensile testing-Part 1: Method of test at room temperature. ISO standard 6892-19; 2019.

[33] ASTM International. Standard test method for linear thermal expansion of solid materials by thermomechanical analysis 1, 2019. doi:10.1520/E0831-19

[34] Corbacho JL, Suárez JC, Molleda F. Grain coarsening and boundary migration during welding of Invar Fe-36Ni Alloy," 1998.

[35] David SA, Vitek JM. Correlation between solidification parameters and weld microstructures. Int Mater Rev. 1989;34(1):213–245. doi:10.1179/imr.1989.34.1.213

[36] ASTM International. Test methods for determining average grain size. Sep. 01, 2021, ASTM International, West Conshohocken, PA. doi:10.1520/E0112-13R21

[37] Lippold J. Welding metallurgy and weldability.

[38] Li Y, Wang J, Han EH, et al. Multi-scale study of ductility-dip cracking in nickel-based alloy dissimilar metal weld. J Mater Sci Technol. 2019;35(4):545–559. doi:10.1016/j.jmst.2018.10.023

[39] Gwalani B, Salloom R, Alam T, et al. Composition-dependent apparent activation-energy and sluggish grain-growth in high entropy alloys. Mater Res Lett. 2019;7(7):267–274. doi:10.1080/21663831.2019.1601644

[40] Zhang H, Li R, Liu J, et al. State-of-art review on the process-structure-properties-performance linkage in wire arc additive manufacturing. Virtual Phys Prototyp. 2024;19(1):2390495. doi:10.1080/17452759.2024.2390495

[41] Chen JQ, Lu H, Cui W, et al. Effect of grain boundary behaviour on ductility dip cracking mechanism. Mat Sci Technol. 2014;30(10):1189–1196. doi:10.1179/1743284713Y.0000000431

[42] Ramirez AJ, Sowards JW, Lippold JC. Improving the ductility-dip cracking resistance of Ni-base alloys. J Mater Process Technol. 2006;179(1–3):212–218. doi:10.1016/j.jmatprotec.2006.03.095

[43] Böllinghaus T, Herold H, Cross CE, et al. Ductility-dip cracking. In: *Hot Cracking Phenomena in Welds II*, Berlin: Springer-Verlag; 2008. p. 389–455.

[44] Böllinghaus T, Herold H. Hot cracking phenomena in welds.

[45] Ramirez AJ, Lippold JC. New insight into the mechanism of ductility-dip cracking in ni-base weld metals. In: Böllinghaus T, Herold H, editors. Hot cracking phenomena in welds. Berlin: Springer-Verlag; 2005. p. 19–41.

[46] Ji L, Lu J, Liu C, et al. Microstructure and mechanical properties of 304L steel fabricated by arc additive manufacturing. in MATEC Web of Conferences, EDP Sciences, 2017. doi:10.1051/matecconf/201712803006

[47] Elliott RO, Kempter CP. Thermal expansion of some transition metal carbides. J Phys Chem. 1958;62(5):630-631. doi:10.1021/j150563a030

[48] Baker A, Dutton S, Kelly D, editors. Composites form and manufacture. In: *Composite materials for aircraft structures*. 2nd ed. 2004; AIAA. p. 113–169.

[49] Nakama K, Sugita K, Shirai Y. Effect of MC type carbides on age hardness and thermal expansion of Fe-36 wt%Ni-0.2 wt%C alloy. Metallogr Microstruct Anal. 2013;2(6):383–387. doi:10.1007/s13632-013-0101-9

[50] TSUDA M. Effect of Minor Alloying Elements on the Mean Thermal Expansion Coefficient of Fe-36% Ni Invar Alloy. Tetsu-to-Hagane. 1994;80(12):944–949. doi:10.2355/tetsutohagane1955.80.12_944

[51] Nelson JB, Riley DP. An experimental investigation of extrapolation methods in the derivation of accurate unit-cell dimensions of crystals. Proc Phys Soc. 1945;57(3):160–177. doi:10.1088/0959-5309/57/3/302

[52] Coey M, Parkin SSP, editors. Handbook of magnetism and magnetic materials. Switzerland: Springer Nature; 2021.

[53] Cullity BD, Graham CD. Magnetostriction and the effects of stress. In: Introduction to Magnetic Materials. 2nd ed. Hoboken: John Wiley & Sons, Inc; 2009. p. 241–275.

[54] Rancourt DG, Dang M-Z. Relation between anomalous magnetovolume behavior and magnetic frustration in Invar alloys. Phys Rev B. 1996;54(17):12225–12231. doi:10.1103/PhysRevB.54.12225

[55] Gorria P, Martínez-Blanco D, Pérez MJ, et al. Stress-induced large Curie temperature enhancement in Fe64 Ni36 Invar alloy. Phys Rev B Condens Matter Mater Phys. 2009;80(6):064421. doi:10.1103/PhysRevB.80.064421

[56] Anand KS, Goswami D, Jana PP, et al. Correlating the lattice parameter and Curie temperature of γ -Ni in Fe-Ni-base alloys. AIP Adv. 2019;9(5):055126. doi:10.1063/1.5097345